

Med-Query: Steerable Parsing of 9-DoF Medical Anatomies with Query Embedding

Heng Guo, Jianfeng Zhang, Ke Yan, Le Lu, *Fellow, IEEE*, and Minfeng Xu

Abstract—Automatic parsing of human anatomies at instance-level from 3D computed tomography (CT) scans is a prerequisite step for many clinical applications. The presence of pathologies, broken structures or limited field-of-view (FOV) all can make anatomy parsing algorithms vulnerable. In this work, we explore how to exploit and conduct the prosperous detection-then-segmentation paradigm in 3D medical data, and propose a steerable, robust, and efficient computing framework for detection, identification, and segmentation of anatomies in CT scans. Considering complicated shapes, sizes and orientations of anatomies, without lose of generality, we present the nine degrees-of-freedom (9-DoF) pose estimation solution in full 3D space using a novel single-stage, non-hierarchical forward representation. Our whole framework is executed in a steerable manner where any anatomy of interest can be directly retrieved to further boost the inference efficiency. We have validated the proposed method on three medical imaging parsing tasks of ribs, spine, and abdominal organs. For rib parsing, CT scans have been annotated at the rib instance-level for quantitative evaluation, similarly for spine vertebrae and abdominal organs. Extensive experiments on 9-DoF box detection and rib instance segmentation demonstrate the effectiveness of our framework (with the identification rate of 97.0% and the segmentation Dice score of 90.9%) in high efficiency, compared favorably against several strong baselines (e.g., CenterNet, FCOS, and nnU-Net). For spine identification and segmentation, our method achieves a new state-of-the-art result on the public CTSpine1K dataset. Last, we report highly competitive results in multi-organ segmentation at FLARE22 competition. Our annotations, code and models will be made publicly available at: [Med-Query](#).

Index Terms—9-DoF Parameterization, Steerable Detection, Detection-then-segmentation, Instance Query.

I. INTRODUCTION

Deep learning based methods have been remarkably successful in various medical imaging tasks [1]. It may be generally believed that models can analyze almost any anatomy with sufficient well-annotated data at hand, if not considering computation burdens. It is also desirable to accurately segment and quantify as many anatomies as possible in clinical practice. For instance, clinicians may use automatically segmented ribs around the target tumor as organs-at-risk in stereotactic body radiation therapy (SBRT) [2]. In opportunistic osteoporosis screening using routine CT, the first lumbar vertebra is the common anatomy of interest [3]. From the computing side, precisely parsing ribs or vertebrae into individual instances and assigning each one with its anatomical label are required,

H. Guo and J. Zhang are with Alibaba DAMO Academy, Hangzhou, 310030, China; K. Yan and M. Xu are with Alibaba DAMO Academy, Beijing, 100026, China; L. Lu is with Alibaba DAMO Academy, New York, NY 10014, USA.

Corresponding author: Minfeng Xu (eric.xmf@alibaba-inc.com).

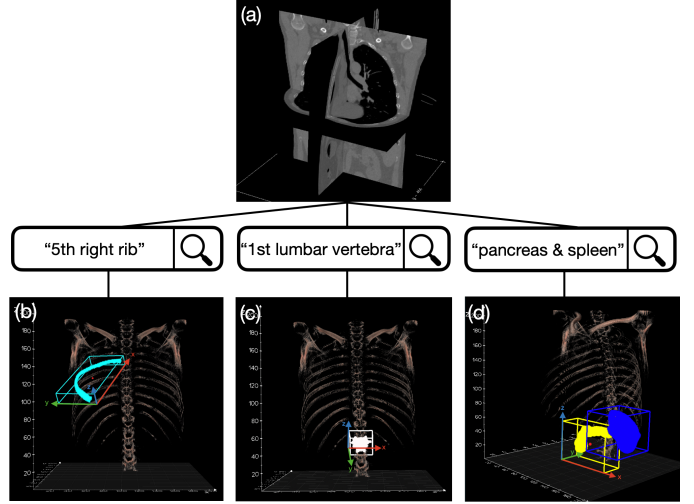


Fig. 1. Illustration of the steerable anatomy parsing concept. (a) Input 3D CT scan. (b) Target rib identified by query. (c) Target vertebra identified by query. (d) Identifying pancreas and spleen simultaneously. Best viewed in color.

e.g., “5th right rib” or “1st lumbar vertebra”. Extensive previous work have been proposed for nearly two decades [4]–[13], among them complicated heuristic parsing rules were constructed in order to obtain robust and holistically valid anatomy labeling results. This motivates us to develop an alternative Transformer [14], [15] based method that can detect, identify, and segment anatomies in a steerable way to bypass the daunting procedure. By *steerable* we mean that we can directly retrieve any anatomy of interest. If the 5th right rib is expected to be analyzed, our framework should output the actual localization and pixel-level segmentation mask of the targeted rib if it exists in the input scan; otherwise output empty. This is illustrated intuitively in Fig. 1.

To achieve this goal, we need an effective deep feature embedding to encode high-level anatomical information including semantic label, location, size, shape, texture, and relation with contextual circumstances. The success of Transformer on natural language processing and its application on object detection in computer vision shed light on the embedding learning [14], [15]. DETR, the first Transformer-based object detector, models object detection as a set prediction problem and uses bipartite matching to bind query predictions with the ground-truth boxes during training [15]. In this work, we explore to utilize some intrinsic properties in medical imaging, such as label uniqueness (e.g., there is only one “5th right rib”), to achieve a steerable detection scheme. An effective weighted adjacency matrix is proposed to guide the bipartite

matching process. Once converged, each query embedding will be attached with an anatomically semantic label, and the model can run in a steerable way. Thus, our model is named Med-Query, i.e., steerable medical anatomy parsing with query embedding.

Detection in full 3D space is non-trivial, especially for repeated anatomical sequential structures, such as ribs or vertebrae. For rib parsing, the first barrier that we have to overcome is how to represent each elongated and oblique rib using a properly parameterized bounding box. The ordinary axis-aligned 3D bounding boxes enclosing ribs will have large portions of overlaps (spatial collisions among nearby boxes), posing additional difficulties for segmentation. To be effective and keep generality, we choose the fully-parameterized 9-DoF bounding box to handle 6D pose and 3D scale/size estimation. This strategy was studied in marginal space learning for heart chambers detection and aortic valve detection [16], [17], and in incremental parameter learning for ileo-cecal valve detection [18]. However, previous methods employed a hierarchical formulation to estimate 9-DoF parameters in decomposed steps. In contrast, we present a direct and straightforward one-stage 9-DoF bounding box detection strategy.

9-DoF bounding box detection task poses a huge challenge for modern detectors if they are based on heuristic anchor assignment [19]–[21], because of the intractable computation expense of intersection-over-union (IoU) in 3D space. It is hard for the widely used post-processing operation of non-maximum suppression (NMS) [22] on 9-DoF bounding boxes to work efficiently for the same reason. However, in our scenario, due to the uniqueness of each anatomy or query, NMS is not essential. Our Med-Query is built upon DETR, a Transformer-based anchor-free detector [15], to predict the box parameters directly, thus circumvents the otherwise necessary IoU and NMS computations. We further extend another two popular anchor-free detectors of CenterNet [23] and FCOS [24] into the 9-DoF setting in our framework to investigate the performance gap between Transformer and convolutional neural network (CNN) architectures. Experimental results show that Transformer-based method empirically exhibits advantages on anatomy parsing problems, which might be attributed to its capability of modeling long-range dependencies and holistic spatial information.

For a comprehensive anatomy parsing task, only detection and identification is not sufficient and pixel-level segmentation is needed in many scenarios. As we know, segmentation task should be addressed in high image resolution to reduce imaging resampling artifacts [25]. However, keeping the whole 3D image in (original) high CT resolution is not computationally efficient. Therefore, detecting to obtain a compact 3D region of interest (ROI) then segmenting to get the instance mask inside ROI becomes the mainstream practice in computationally efficient solutions [16], [17], [26]–[29], which we also follow.

In this work, we present a unified computing framework for a variety of anatomy parsing problems, with ribs, spine, and abdominal organs as examples. Our method consists of three main stages: task-oriented ROI extraction, anatomy-specific 9-DoF ROI detection, and anatomy instance segmentation. Input 3D CT scans are operated at different resolutions in different

processing stages. ROI extractor is trained and tested at an isotropic spacing of 3mm, detector is conducted at 2mm, and the segmentation network is conducted at the original CT spacing of the input volume with the finest image resolution. The whole inference latency is around 3 seconds per CT scan on an NVIDIA V100 GPU, outperforming several highly optimized methods [9], [25] in the rib parsing task. If we query only a subset of all ribs instead, the needed computing time can be further shortened.

In addition, among these three anatomical structures utilized in this work, ribs relatively lack of high quality publicly available dataset. Thus this instance parsing problem has not been as extensively studied as the other two tasks [10]. To address this issue, we curate an elaborately annotated instance-level rib parsing dataset, named RibInst, substantially built upon a previously released chest-abdomen CT dataset of rib fracture detection and classification [30]. RibInst will be made publicly available to the community by providing a standardized and fair evaluation benchmark for future rib instance segmentation and labeling methods.

Our main contributions are summarized as follows.

- We present a Transformer-based Med-Query method for simultaneously estimating and labeling 9-DoF ROI of anatomy in CT scans. To the best of our knowledge, we are the first to estimate the 9-DoF representation in 3D medical imaging using a one-stage Transformer.
- A steerable object/anatomy detection model is achieved by proposing an effective weighted adjacency matrix in the bipartite matching process between query and ground-truth boxes. This steerable attribute enables a novel medical image analysis paradigm that permits to directly retrieve any instance of anatomy of interest and further boost the inference efficiency.
- We propose a unified computing framework that can generalize well for a variety of anatomy parsing problems. This framework achieves new state-of-the-art quantitative performance results on detection, identification and segmentation of anatomies, comparing to other strong baseline methods.
- Last but not least, we will release publicly a comprehensively annotated instance-level rib parsing CT dataset of 654 patients, termed RibInst, built on top of a previous chest-abdomen CT dataset [30].

II. RELATED WORK

Detection, identification and segmentation. Automated parsing techniques have been widely adopted for object/anatomy detection, identification and segmentation in medical imaging domain [1], [31], [32]. From the specific application perspective, previous work can be roughly categorized into task-specific and universal methods. In rib parsing, existing methods solve rib segmentation and labeling relying heavily on seed points detection and centerline extraction, thus its results can be inaccurate or even fail when seed points are missing or mis-located [4]–[6], [9]. Using auxiliary representations for parsing ribs are also explored: skeletonized centerlines [7], [8] or point cloud [10]. Similarly in spine parsing, complicated

heuristic rules or sophisticated processing pipelines [11]–[13], [33] are often constructed in order to obtain robust labeling results. Recent end-to-end segmentation neural network models demonstrate their versatility so that have been widely adopted, such as U-Net [34], [35], V-Net [36], and so on. Particularly, nnU-Net [25] and its variants have achieved cutting-edge performances in various medical imaging segmentation tasks [37]–[40]. All existing techniques do not offer steerable 3D object/anatomy detection as query retrieval. In this work, we present a unified computing framework that can generalize well for a variety of anatomy parsing tasks, based on the detection-then-segmentation paradigm in 3D medical image analysis with steerable, robust and efficiency benefits.

Detection-then-segmentation paradigm has dominated the instance segmentation problem in photographic images. He et al. [26] extend Faster R-CNN [19] to Mask R-CNN by adding a branch for predicting the segmentation mask of each detected ROI. Several work emerge from Mask R-CNN, e.g., PANet [27], HTC [28] and QueryInst [29]. There are some other work that do not rely on the explicit detection stage [41]–[43]. The detection-then-segmentation paradigm deserves to be exploited further in 3D medical imaging data where precision and computation efficiency both matter. For rib instance segmentation, previous techniques can not be directly applied since the ribs are orientated obliquely and are so close to neighbouring ones that these regular axis-aligned bounding boxes would be largely overlapped. Partially inspired by [16] and [18], in which 9-DoF parameterized boxes are employed to localize the target region with a hierarchical workflow to estimate the box parameters progressively, we parametrically formulate the detection target for each rib as a 9-DoF bounding box encompassing the rib tightly. This 9-DoF representation can be generalized to other anatomies existing in 3D medical imaging volumes. Direct 9-DoF box estimation on point clouds have been explored recently [44]–[46], demonstrating promising results on this complex pose estimation problem in 3D space. In this work, we tackle the similar task by detecting the 9-DoF bounding box of anatomy in one-stage using 3D CT scans.

Anchor-free object detection techniques have been well studied [15], [23], [24], [47]–[52]. YOLO [47] reports comparable detection performance close to Faster R-CNN [19] while running faster. Several anchor-free methods also obtain competitive accuracy with high inference efficiency. Zhou et al. [23] present CenterNet that models an object as the center point of its bounding box so that object detection is simplified as key point estimation and size regression. FCOS [24] takes advantage of all points in a ground-truth box to supplement positive samples and suppresses the low-quality detected boxes with its “centerness” branch. Apart from CNN based methods, DETR [15] comes up with a new representation that views object detection as a direct set prediction problem with Transformer. It learns to produce unique predictions via the bipartite matching loss and utilizes global information with the self-attention mechanism [14], beneficial for the detection of large or elongated objects. More recently, 3DETR [53] of a detection model for 3D point clouds has proven that the Transformer-based detection paradigm can be extended to 3D space with

minor modifications and achieve convincing results with good scalability in dealing with higher dimensional object detection problems.

III. APPROACH

A. Problem Definition

Anatomy parsing focuses on distinguishing each instance in a cluster of similar anatomical structures with a unique anatomical label, e.g., recognizing each rib in a ribcage, splitting each vertebra in a spine, and delineating each organ in the abdominal region in 3D CT scans. Our work distinguishes itself from existing work on its steerable capability that is attributed to a Transformer-based 9-DoF box detection module. We briefly describe our overall detection framework as follows. Giving a CT scan containing $N(1 \leq N \leq C)$ targets, C is the maximum number of target anatomies in normal scan (e.g., C is set as 24 for rib parsing in our work according to [54]), the whole anatomy set can be expressed as $x = \{x_i = (c_i, x_i^p, x_i^s, x_i^a), 1 \leq i \leq N\}$, where c_i, x_i^p, x_i^s, x_i^a stands for anatomy instance label, center position component, scale component, and angle component of the correspondingly parameterized bounding box, respectively. The goal of the detection task is to find the best prediction set \hat{x} that matches x for each object/organ/anatomy instance. Unless specified otherwise, the term *position* in the following context refers to the position of the box center.

B. 9-DoF Box Parameterization

To get a compact parameterization for anatomy localization, we compute the 9-DoF bounding box via principle component analysis (PCA) [56], based on the annotated instance-level 3D segmentation mask. Specifically, three steps are performed: 1) computing eigenvalues and eigenvectors of covariance matrix, based on the voxel coordinates of each anatomy mask; 2) sorting eigenvalues to determine the axes for the local coordinate system with the correspondent eigenvectors; 3) formulating the 9-DoF box in representation of $(x, y, z, w, h, d, \alpha, \beta, \gamma)$ based on the anatomy mask and the local coordinate system. To be more specific, (x, y, z) stands for the box center and is transformed back into the world coordinate system to keep invariance whenever any data augmentation applies; (w, h, d) represents for the box scale along x -axis, y -axis, and z -axis of the local coordinate system, respectively, and is stored in the unit of millimeter; (α, β, γ) stands for the box’s Euler angles around Z -axis, Y -axis, and X -axis of the world coordinate system, respectively. An intuitive visual illustration can be found in Fig. 1. It is noteworthy that this universal parameterization can be customized to be degraded or simplified, e.g., only keeping the angle of pitch as the rotation parameter may be sufficient to define the vertebra parameterization (Fig. 1(c)), depending on the specific anatomical characteristics.

C. Med-Query Architecture

In this section, we describe our full architecture in details. Based on the steerable anatomy detector, we also enhance our algorithm pipeline with a preceding task-oriented ROI

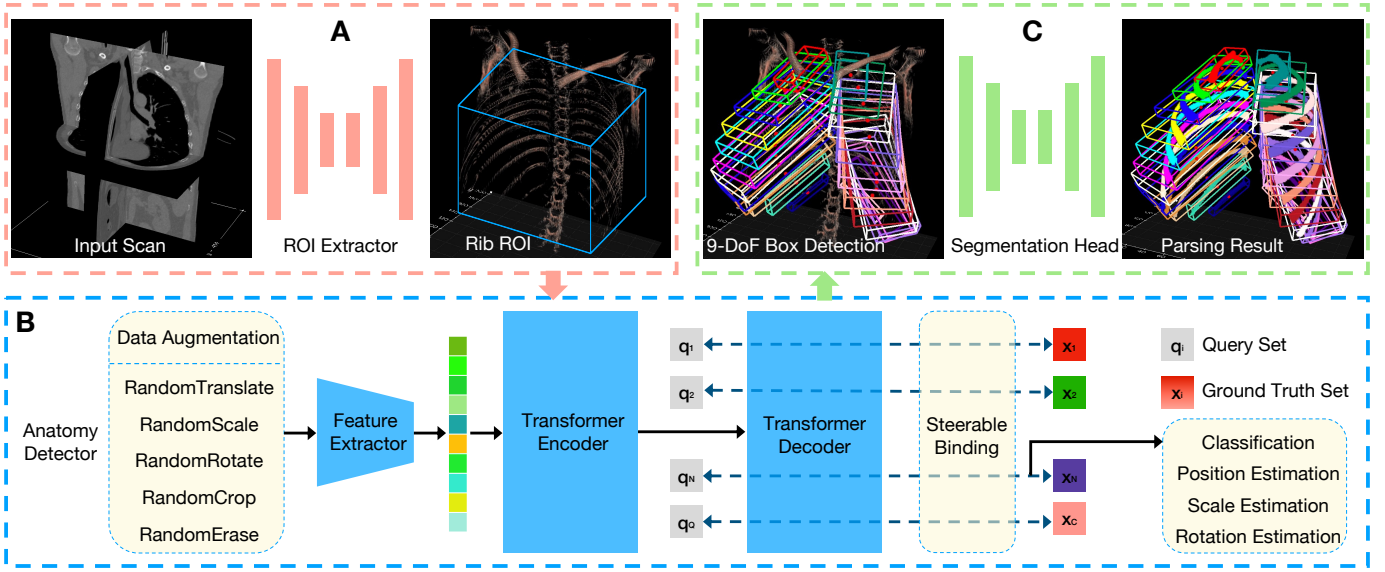


Fig. 2. An instantiation of Med-Query architecture for rib parsing, which consists of **A**: a ribcage ROI extractor, **B**: a steerable 9-DoF parametric rib detector, and **C**: a stand-alone segmentation head, for robust and efficient rib parsing, i.e., instance segmentation and labeling. In **(B)** Anatomy Detector, we use an adapted 3D version of ResNet [55] as feature extractor. The stacked colored illustrative blocks next to the feature extractor represents the flattened spatial features.

extractor and a subsequent stand-alone segmentation head. The term “Med-Query” is not limited to the detector itself but represents the whole processing framework. For ease of illustration, a schematic flowchart on a concrete application example of rib parsing, is demonstrated in Fig. 2.

ROI Extractor. The scales and between-slice spacings of chest-abdomen CT scans vary greatly. To make Med-Query concentrated in the target rib region, a task-oriented ROI extraction which involves only ribcage area would be helpful. Simply thresholding to get the ROI is not robust, especially for input scans with large FOVs, e.g., from neck to abdomen. To obtain an accurate ROI estimation when handling with input CT scans under various situations, we train a simplified U-Net [34] model to coarsely identify the rib regions in 3D, then the proper ROI box can be inferred by calculating the weighted average coordinates and distribution scope of the predicted rib voxels. At inference stage, the obtained ROI center is critical and the ROI scale can be adjusted depending on the data augmentation strategies adopted in training. Our ROI extractor is computationally efficient while running on an isotropic spacing of $3mm \times 3mm \times 3mm$.

Steerable Anatomy Detector. DETR [15] handles object detection as a direct set prediction problem through the conjunction of the bipartite matching loss and Transformer [14] with parallel decoding of queries. Queries in DETR demonstrate the preference on object spatial locations and sizes in a statistical perspective. If there exists a deterministic binding between the learned query embedding and anatomical structures, a steerable object parsing paradigm for medical imaging is achievable. Medical imaging differs from natural images mainly in two aspects: 1) the semantic targets inside medical imaging scans are relatively more stable with respect to their quantities and absolute/relative positions, even though there exist some local ambiguities; 2) the anatomical label

for each instance is unique. These two intrinsic properties constitute the cornerstones of developing a steerable anatomy detector. The remaining obstacle is how to obtain a deterministic/steerable binding.

We empirically find that the model can be trapped in random bindings between queries and ground-truth boxes due to different initialization parameters. Two simple examples are illustrated in Fig. 3(a)(b). We take this one step further and intend to fix the binding consequence, as in Fig. 3(c). We define the query set as $q = \{q_i, 0 \leq i \leq Q\}$. Note that in our experiments, the total number of queries is set as $C + 1$, which is the number of output channels for the classification branch in each query prediction, with the channel zero as the background class.

To explicitly guide the bipartite matching process, we propose a weighted adjacency matrix $M \in \mathbb{R}^{(Q+1) \times (Q+1)}$, which can be interpreted as an index cost term to penalize the index mismatch between queries and ground-truth boxes. A matrix instantiation with 10 queries is shown in Fig. 3(d), as can be seen, the greater the index gap, the higher the index cost. Therefore, assuming a query with index $\sigma(i)$ and its prediction $\hat{x}_{\sigma(i)}$, our matching cost on $(\hat{x}_{\sigma(i)}, x_i)$ can be defined as:

$$\begin{aligned} C(\hat{x}_{\sigma(i)}, x_i) = & -\lambda_c \hat{p}_{\sigma(i)}(c_i) + \lambda_p \|\hat{x}_{\sigma(i)}^p - x_i^p\|_1 \\ & + \lambda_s \|\hat{x}_{\sigma(i)}^s - x_i^s\|_1 + \lambda_a \|\hat{x}_{\sigma(i)}^a - x_i^a\|_1 \quad (1) \\ & + \lambda_m M[\sigma(i), c_i], \end{aligned}$$

where c_i is the target class label, $\hat{p}_{\sigma(i)}(c_i)$ is the probability prediction on class c_i , and $\lambda_c, \lambda_p, \lambda_s, \lambda_a, \lambda_m$ are cost coefficients for classification, position, scale, rotation, and the preset weighted adjacency matrix, respectively. In our implementation, the position values and scale values in the image coordinate system are normalized by the image size $[W, H, D]$, thus they can be merged into the same branch with a *sigmoid* function as its activation.

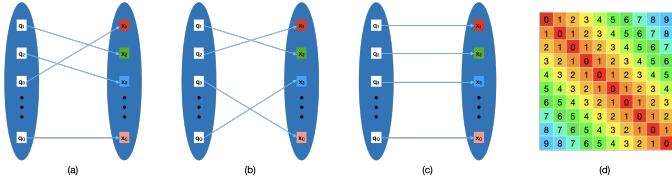


Fig. 3. Three types of binding results between queries and ground-truth boxes: (a), (b) and (c). (d) shows an instantiation of the weighted adjacency matrix with 10 queries and 10 ground-truth classes. Queries are arranged in rows while ground-truths are arranged in columns.

The optimal matching $\hat{\sigma}$ is searched using Hungarian algorithm [57]. Then our loss function is defined similarly as:

$$\mathcal{L}(\hat{x}, x) = \frac{1}{N} \sum_{i=1}^N \left[-\lambda_c \log \hat{p}_{\hat{\sigma}(i)}(c_i) + \lambda_p \|\hat{x}_{\hat{\sigma}(i)}^p - x_i^p\|_1 + \lambda_s \|\hat{x}_{\hat{\sigma}(i)}^s - x_i^s\|_1 + \lambda_a \|\hat{x}_{\hat{\sigma}(i)}^a - x_i^a\|_1 \right], \quad (2)$$

where the coefficients are kept consistent with those in Eq. (1). For queries matched to the background class, only the classification loss is accounted. Note that we merely use L1 Loss for the geometrical 9-DoF box regression. No IoU-related loss [58] is used in bipartite matching or loss computing, which is different from [15] and [53]. The proposed preset matrix only takes effects at the matching stage.

Segmentation Head. The input data for the aforementioned detector is isotropic with the spacing of $2mm \times 2mm \times 2mm$ per voxel which is finer than the ROI extraction step. To obtain high accuracy instance segmentation results with affordable training expense, we adopt a stand-alone U-Net [34] to segment each anatomy independently with a finer spatial resolution in a locally cropped FOV. Specifically, each detected 9-DoF bounding box from our steerable anatomy detector is expanded slightly to crop a sub-volume from the input CT volume at the original spacing. Then the segmentation head performs a binary segmentation for all sub-volumes, with the anatomy of interest being segmented as foreground and other tissues (including neighbouring anatomies of the same category) as background. After this, all predicted binary masks are merged back with their corresponding labels and spatial locations into the original CT scan coordinate system to form the final instance segmentation output. Our detector and segmentation head is designed to be disentangled, so there are good flexibility and scalability to employ even more powerful segmentation networks than [34]. Furthermore, benefiting from the steerable nature of the proposed detector, the segmentation head can be invoked dynamically per detection box at request, to save computational cost if necessary.

D. Data Augmentation

For better model generalization and training efficiency, we employ both online and offline data augmentation schemes.

Offline Scheme. We perform *RandomCrop* along Z -axis to imitate (largely) varying data input FOVs in realistic clinical situations, where FOVs can contain or cover the targeted object/anatomy region completely or only partially. Spatial cropping may truncate some obliquely oriented anatomies,

whose 9-DoF parameterization need to be recomputed. Online computation is time-consuming so that we conduct this operation offline.

Online Schemes. Since the anatomy position, orientation and scale vary case by case, local spatial ambiguities exist among different CT scans, posing great challenges for identifying each anatomy correctly and precisely. We perform 3D *RandomTranslate*, *RandomScale*, and *RandomRotate* to add more input variations and alleviate this problem. These operations can be conducted efficiently without 9-DoF box recomputation, so they are performed online during the training process. According to [54], 5%-8% of normal individuals may have 11 pairs of ribs. This raises an obstacle because we have no sufficient training data exhibiting this pattern of anatomy variation. Hence, for rib parsing task, we particularly use *RandomErase* to remove the bottom pair of ribs in the training set with a certain probability ratio, to alleviate the possible over-prediction problem. No additional data augmentation is used otherwise.

IV. EXPERIMENTS

A. Datasets

RibInst dataset is constructed from a public CT dataset that was used as the rib fracture evaluation benchmark in *RibFrac* challenge [30]. This original dataset consists of total 660 chest-abdomen CT scans with 420 for training, 80 for validation and 160 for testing. We comply with the dataset splitting rule and annotate each rib within each CT scan with spatially ordered and unique labels. There are 6 cases with extremely incomplete FOV in the validation set, infeasible to identify the correct rib labels. Therefore RibInst dataset has the remaining 654 CT scans. Note that a dataset with 490 CT scans annotated with binary rib segmentation masks and labeled rib centerlines was released [10]. Compared with it, RibInst is more concise and comprehensive, for conducting rib instance segmentation evaluation without centerline extraction.

CTSpine1K provides 1,005 CT scans with instance-level vertebra annotation for spine analysis [39], [59]. The dataset is curated from four previously released datasets ranging from head-and-neck imaging to colonography scans. It serves as a benchmark for spine-related image analysis tasks, such as vertebrae segmentation and labeling. There are 610 scans for training and the remaining are for validation and testing.

FLARE22 stands for Fast and Low-resource semi-supervised Abdominal oRgan sEgmentation in CT, a challenge held in MICCAI 2022. The dataset is curated from three abdomen CT datasets. The segmentation targets contain 13 organs: liver, spleen, pancreas, right kidney, left kidney, stomach, gallbladder, esophagus, aorta, inferior vena cava, right adrenal gland, left adrenal gland, and duodenum. As a semi-supervised task, the training set includes 50 labeled CT scans with pancreas disease and 2,000 unlabeled CT scans with liver, kidney, spleen, or pancreas diseases. There are also 50 CT scans in the validation set and 200 CT scans in the test set with various diseases. For more information, readers are referred to the challenge website¹.

¹<https://flare22.grand-challenge.org>

B. Implementation Details

Our implementation uses PyTorch [60] and is partially built upon MMDetection [61]. The detector in Med-Query is trained with AdamW optimizer [62] in the initial setting of $lr = 4e-4$, $\beta_1 = 0.9$, $\beta_2 = 0.999$, $weight_decay = 0.1$. The total training process contains 1000 epochs: the first 200 epochs to linearly warm up and the learning rate lr is reduced by a factor of 10 at the 800th epoch. It costs about 20 hours on 8 V100 GPUs with a single GPU batch size of 8. We empirically set coefficients $\lambda_c = 1$, $\lambda_p = 10$, $\lambda_s = 10$, $\lambda_a = 10$, $\lambda_m = 4$. The network output of the fourth stage (C4), from an adapted 3D ResNet50 is used as the spatial features for Transformer encoding. The Transformer component consists of a one-layer encoder and a three-layer decoder, which is empirically found to be sufficient in our task. We follow [53] to set a dropout of 0.1 in encoder and 0.3 in decoder. The MultiHeadAttention block of both have 4 heads. The length of positional encoding in one-axis is set as 128, thus the total embedding dimensions is 384 in our case. We use data augmentations mentioned in Section III-D to generate diverse training data offline and on the fly, the maximum translation distance from the reference center (i.e., anatomy mask center in our experiments) is 20mm, the scaling range is [0.9, 1.1], and the rotation range is $[-15^\circ, 15^\circ]$. The ROI extractor and segmentation head are trained separately, for the sake of training efficiency. All models in our experiments are trained from scratch.

C. Performance Metrics

Detection and Identification. To evaluate the 9-DoF box detection and identification performance, we refer to the practice of *VerSe* [13], a vertebrae labeling and segmentation benchmark. We extend the Identification Rate (Id.Rate) computation in *VerSe* by considering all factors of the label accuracy, center position deviation (P_{mean}), scale deviation (S_{mean}) and angle deviation (A_{mean}), to evaluate 9-DoF box predictions from different methods. To be more specific: giving a CT scan containing N ground-truth anatomy boxes and the true location of the i^{th} anatomy box denoted as x_i with its predicted box denoted as \hat{x}_i (M predictions in total), the anatomy i is correctly identified if \hat{x}_i among $\{\hat{x}_j \forall j \in \{1, 2, \dots, M\}\}$ is the closet box predicted to x_i and subjects to the following conditions:

$$\begin{cases} \|\hat{x}_i^p - x_i^p\|_2 < 20 \text{ mm}, \\ (\sum_{k=1}^3 \|\hat{x}_i^{s_k} - x_i^{s_k}\|_1)/3 < 20 \text{ mm}, \\ (\sum_{k=1}^3 \|\hat{x}_i^{a_k} - x_i^{a_k}\|_1)/3 < 10^\circ, \end{cases} \quad (3)$$

where the superscript p denotes the center position component of the box, the superscript s_k denotes the scale component in axis k , and the superscript a_k represents the Euler angle component rotated around axis k . Given a CT scan, if there are R anatomies correctly identified, then Id.Rate is defined as $\text{Id.Rate} = \frac{R}{N}$. The center position deviation is computed as $P_{\text{mean}} = (\sum_{i=1}^R \|\hat{x}_i^p - x_i^p\|_2)/R$. Similarly, the scale deviation is computed as $S_{\text{mean}} = (\sum_{i=1}^R \sum_{k=1}^3 \|\hat{x}_i^{s_k} - x_i^{s_k}\|_1)/3R$, and the angle deviation is computed as $A_{\text{mean}} = (\sum_{i=1}^R \sum_{k=1}^3 \|\hat{x}_i^{a_k} - x_i^{a_k}\|_1)/3R$. Note that we only compute

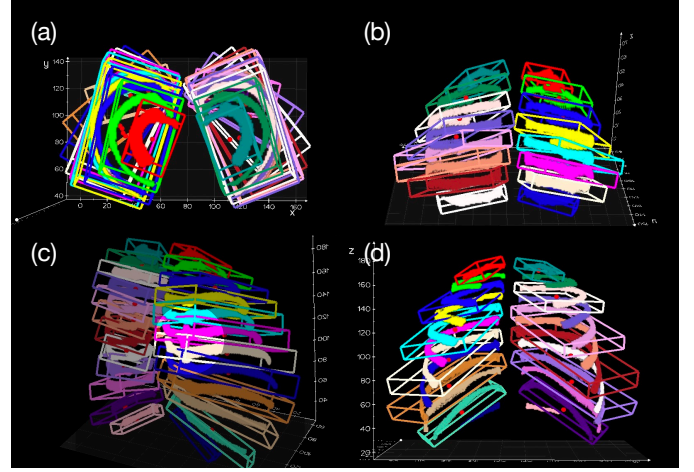


Fig. 4. Detection visualizations show that our 9-DoF predictions enclose the ground-truth rib masks accurately. (a) Normal results in superior-to-inferior view. (b) A limited FOV case in posterior-to-anterior view. (c) A case with rib adhesions. (d) Only odd-number labels are queried. Ground-truth masks are rendered as visual reference.

the average deviations of the identified anatomies where unpredicted anatomies or mislocated predictions have been reflected by the Id.Rate index.

Segmentation. We employ the widely-used Dice similarity coefficient (DSC), 95% Hausdorff distance (HD95) and average symmetric surface distance (ASSD) as segmentation metrics. For missing anatomies, HD and ASSD are not defined. We follow the practice of [13] to ignore such anatomies when computing the averages. Those missing anatomies will be reflected on DSC and Id.Rate. We utilize a publicly available evaluation toolkit² to compute the surface measures.

D. Main Results

We report comprehensive evaluation results on RibInst from rib instance detection and segmentation. Besides, we validate the performance generality of our framework on CTSpine1K and FLARE22 datasets, and report the segmentation performances compared with several strong baseline methods.

Detection Evaluation on RibInst. From Table I, Med-Query achieves the best identification rate of 97.0% with a moderate amount of parameters. The capability of capturing long-range dependencies and holistic information of Transformer appears to be suitable at solving this sequence modeling problem. Notably, compared with pure CNN architectures, Med-Query can infer at least 10x faster in terms of latency. This may benefit from not relying on additional upsampling layers in [23] or dense prediction heads in [24]. Meanwhile, we have some interesting findings on different characteristics of Med-Query and traditional object detectors [23], [24] that recognize objects individually while ignoring relations between objects [65]. In our case, the main reason why FCOS and CenterNet could fail is that they sometimes assign different labels to the same rib or same label to different ribs, subsequently leading to missing ribs as shown in Fig. 5. These traditional detectors did not explicitly consider the anatomy uniqueness

²<https://github.com/deepmind/surface-distance>

TABLE I

Detection and identification results on the test set of RibInst. *Note that CenterNet and FCOS demonstrated here are significantly developed and modified to fit into our task and equipped with the proposed 9-DoF box representation.

Methods	#params(M)	Id.Rate(%) \uparrow	P_{mean} (mm) \downarrow	S_{mean} (mm) \downarrow	A_{mean} ($^{\circ}$) \downarrow	Latency(s) \downarrow
CenterNet* [23]	1.3	94.9	3.032	2.333	2.890	2.575
FCOS* [24]	19.4	94.1	3.100	2.516	1.786	0.745
Med-Query	9.6	97.0	4.702	2.784	2.185	0.065

TABLE II

Segmentation results on the validation set and test set of CTSpine1K. The results of nnFormer, nnU-Net, and CPTM are quoted from [39].

Methods	DSC(%) \uparrow	HD(mm) \downarrow	ASSD(mm) \downarrow
nnFormer [63]	74.3	11.56	-
nnU-Net [25]	84.2	9.02	-
CPTM [39]	84.5	9.03	-
Med-Query	85.0	8.68	1.16

TABLE III

Organ-specific DSC (%) on the validation set of FLARE22. Abbreviations: “RK”-Right Kidney, “IVC”-Inferior Vena Cava, “RAG”-Right Adrenal Gland, “LAG”-Left Adrenal Gland, “Gall.”-Gallbladder, “Eso.”-Esophagus, “Stom.”-Stomach, “Duode.”-Duodenum, “LK”-Left Kidney, “ens.”-ensemble, “pre.”-pre-training, “mDSC”-mean DSC.

Methods	Liver	RK	Spleen	Pancreas	Aorta	IVC	RAG	LAG	Gall.	Eso.	Stom.	Duode.	LK	mDSC \uparrow
nnU-Net [25]	97.7	94.1	95.8	87.2	96.8	87.8	83.0	80.1	76.5	89.2	89.9	77.1	91.1	88.2
nnU-Net ens.	97.9	94.8	96.0	88.6	96.9	89.7	83.8	81.9	78.7	90.1	90.7	79.2	92.0	89.2
Swin UNETR [64]	96.5	91.2	94.2	84.6	93.0	86.5	75.8	74.2	77.1	79.0	88.6	76.5	88.7	85.0
Swin UNETR pre.	96.4	92.1	95.2	88.1	93.7	86.2	79.4	79.1	79.2	81.8	89.5	79.0	87.9	86.7
Med-Query	98.0	94.5	97.2	89.0	96.6	90.3	82.4	80.6	86.1	87.4	91.5	78.7	93.7	89.7

and spatial relationship/dependency between rib labels. Med-Query behaves in another way that solves a label assignment problem rather than an unconstrained object detection task, so that the relations between targets are explicitly constructed and enforced through the steerable label assignment strategy and the intrinsic self-attention mechanism in Transformer models [14]. On the other hand, Med-Query is slightly inferior in local regression indicators as shown in Table I. Med-Query can correctly identify more ribs with global information, but including those challenging ribs in the calculation of deviations may deteriorate the quantitative performances on localization errors. It is noteworthy that all these optimized models achieved small regression deviations w.r.t. P_{mean} , S_{mean} , and A_{mean} . Note that we have improved FCOS and CenterNet with our one-stage 9-DoF detection strategy. The above results demonstrate that the challenging 9-DoF parameter estimation problem can be solved effectively. Some qualitative results of Med-Query in rib detection and labeling are shown in Fig. 4. Our 3D detection visualization tool is developed based on *vedo* [66].

Segmentation Evaluation on RibInst. As shown in Table IV, the widely-used self-configuring nnU-Net [25] achieves a good DSC of 89.7% with a long latency of 252 seconds. nnU-Net is trained with sampled patches, therefore the lack of global information leads to noticeable label confusion, significantly revealed by HD95 of 4.498 mm. We also reimplement a centerline-based method [9] to investigate how the parsing results relies heavily on centerline extraction and heuristic rules. Among all listed methods in Table IV, Med-Query achieves the best DSC of 90.9%. Notably, the whole pipeline of Med-Query can be finished in 2.591 seconds. The efficiency is attributed to our detection-then-segmentation paradigm which detects on low resolution with global FOV and segments on high resolution with local FOV. A qualitative comparison on a representative patient case with rib fractures is shown in Fig. 5, demonstrating the robustness of Med-Query.

Segmentation Evaluation on CTSpine1K. To be aligned

with the evaluation protocol in [39], we report segmentation metrics on vertebra-level average scores computed on all scans in the validation and test set (HD is employed instead of HD95). As in Table II, we compare Med-Query with several strong baselines, including nnFormer [63], nnU-Net [25], and CPTM [39]. Med-Query obtains marked performance improvements on both DSC and HD, achieving a new state-of-the-art result for this challenging task of CTSpine1K. Note that the semi-supervised annotation curation procedure of this dataset used nnU-Net in-the-loop.

Segmentation Evaluation on FLARE22. We report the evaluation results on FLARE22 validation leaderboard that gives the detailed performance evaluation at organ-level. In Table III, nnU-Net and its ensemble version are merely trained on labeled data, as shown, they can achieve very good results on the validation set even with only 50 labeled data. The ensembled nnU-Net (assembly of 12 models from different settings and different folds in cross-validation) can obtain a 1% improvement on mean DSC. Considering the semi-supervised setting of this task, we use nnU-Net as the teacher model to generate pseudo labels for the unlabeled part of the training set, as a straightforward but effective semi-supervised strategy. Based on this, we exploit the performance of a recent published model Swin UNETR [64] on this task. As can be seen, Swin UNETR with self-supervised pre-training on unlabeled data has a 1.7% improvement against its vanilla version. Our method compares favorably with the average DSC of 89.7%, which is a competitive result ranking in top 3% among all 1,162 entries in the validation leaderboard without heavy model ensembles.

E. Ablation Study

We perform ablation study on RibInst to investigate the effectiveness of three key factors in our framework.

Effects of the Weighted Adjacency Matrix. To validate the efficacy of the preset weighted adjacency matrix, we conduct

TABLE IV

Segmentation results on the test set of RibInst. †A centerline-based method proposed in [9]. *Adapted versions, also equipped with ROI extractor and segmentation head.

Methods	DSC(%) \uparrow	HD95(mm) \downarrow	ASSD(mm) \downarrow	Latency(s) \downarrow
Centerline \dagger	84.6	13.84	3.437	18.50
CenterNet*	89.5	1.826	0.725	4.793
FCOS*	88.1	1.137	0.352	3.241
nnU-Net	89.7	4.498	0.900	252.0
Med-Query	90.9	1.644	0.438	2.591

TABLE V

Id.Rate evaluations in different operations and different measurement thresholding combinations. *RandomTranslate*, *RandomScale*, and *RandomRotate* are performed jointly, thus are abbreviated as ‘‘T.S.R’’. ‘‘Re.Dist.’’ represents relative distance constraints. ‘‘PE’’ is short for positional encoding.

No Aug.	Data Aug.			Re.Dist.	w/o PE	20mm20mm	10mm10mm	10mm10mm
	T.S.R	Crop	Erase			10 $^\circ$	10 $^\circ$	5 $^\circ$
\checkmark						83.1	49.0	33.7
	\checkmark					94.4	84.8	79.2
	\checkmark	\checkmark				96.2	89.0	84.2
	\checkmark	\checkmark	\checkmark			96.5	90.7	87.0
	\checkmark	\checkmark	\checkmark	\checkmark		97.0	91.8	87.4
	\checkmark	\checkmark	\checkmark	\checkmark	\checkmark	96.2	92.0	87.9

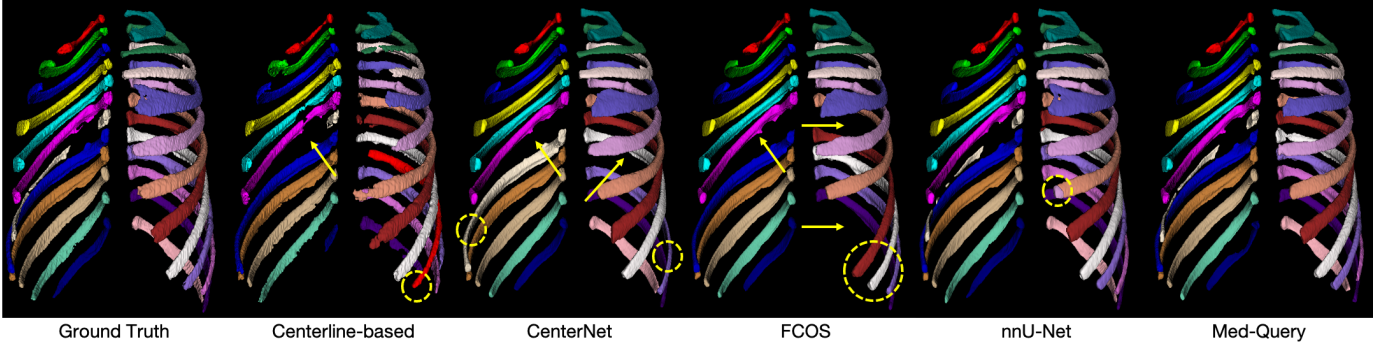


Fig. 5. An example with broken structures in RibInst. Missing or wrong labels are marked using golden arrows and dashed circles, respectively.

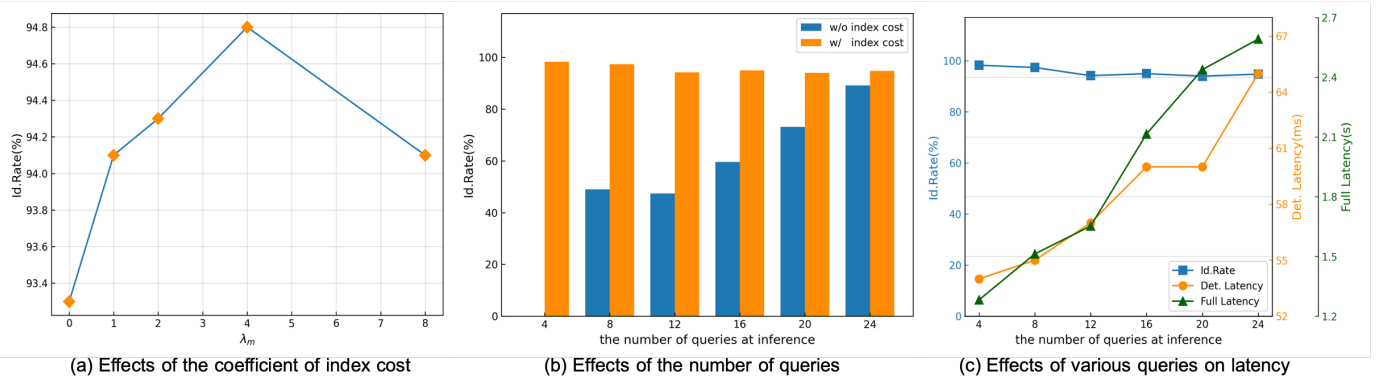


Fig. 6. Ablation studies on the coefficient of the proposed index cost and the number of query embeddings at inference.

an ablation study w.r.t. λ_m , the scaling factor of the matrix, which is also known as index cost. Candidate parameter is chosen from $[0, 1, 2, 4, 8]$ where 0 means the vanilla bipartite matching. We should notice that when λ_m is large enough, it can be regarded as directly assigning the query to a fixed ground-truth label. Fig. 6(a) reveals that a proper value of $\lambda_m = 4$ stands out with the highest Id.Rate of rib labeling. One explanation is that a reasonable perturbation term during the matching process could gradually impose anatomical semantic labels on queries and help build the correct relations among them.

Steerable at Inference? To further validate the steerable attribute of the proposed model, we randomly pick some rib labels with varied number from 4 to 24 with a step size of 4 at inference. The task is to retrieve the pre-selected ribs

with query embeddings in the same sequence where Id.Rate for the given subset of ribs is the evaluation metric. Fig. 6(b) demonstrates the performances of two different settings of with index cost or without index cost. Note that in the round of only 4 ribs are expected to be detected, the model without index cost misses all targets. This is not out of expectation, because the one-to-one relations between query series and ground-truth sequence are not explicitly constructed. As the number of queries increases, the vanilla model can gradually return some correct targets back. On the contrary, Med-Query has a stable performance when the number of query varies. In terms of inference efficiency, Med-Query can be further boosted with less queries required, e.g., if 4 queries are required, it can save 17% of time in detection stage and the ratio can even expand to 50% in the perspective of full pipeline, as shown

in Fig. 6(c). The efficiency improvement benefits from less computation in Transformer decoder and segmentation head when fewer queries are executed. During the above ablation experiments, cropped data is not used.

Data Augmentation & Beyond. We conduct comprehensive experiments to analyze the critical factors in our proposed framework as shown in Table V. The joint operations of *RandomTranslate*, *RandomScale*, and *RandomRotate* in 3D space get the most significant performance gain. *RandomCrop* along *Z*-axis for imitating limited FOVs in clinical practice can further improve the Id.Rate by 1.8%. *RandomErase* gets additional performance benefit. We also explore a common trick of imposing relative distance constraints between neighboring center points in landmark detection tasks [67], and obtain a gain of 0.5%. Additionally, we exploit the efficacy of a 3D extended version of the fixed *Sine* spatial positional encoding that has proven to be useful in [15]. It can be seen that cancellation of this leads to 0.8% Id.Rate drop if the measurement thresholding is set to (20mm, 20mm, 10°). However, if the thresholding is set more strictly, drop will disappear and even get the opposite results. A similar observation that removing positional encoding only degrades accuracy by a small margin can be found in [68]. It implies that positional encoding may deserve further investigation especially in 3D scenarios.

V. CONCLUSION

In this work, we have presented a steerable, robust and efficient Transformer-based framework for anatomy parsing in CT scans. The pipeline is conducted via following the detection-then-segmentation paradigm and processing input 3D scans at different resolutions progressively. To our best knowledge, this work is the first to estimate the 9-DoF representation for object detection in 3D medical imaging via one-stage Transformer. The resulted method can be executed in a steerable way to directly retrieve any anatomy of interest and further boost the inference efficiency. It is a unified computing framework that can generalize well for a variety of anatomy parsing tasks and achieves new state-of-the-art performance on anatomy instance detection, identification and segmentation. We will release our annotations, code and models upon publication, hoping to benefit the community and facilitate the future development on automatic parsing of anatomical structures.

REFERENCES

- [1] X. Chen, X. Wang, K. Zhang, K.-M. Fung, T. C. Thai, K. Moore, R. S. Mannel, H. Liu, B. Zheng, and Y. Qiu, "Recent advances and clinical applications of deep learning in medical image analysis," *Medical Image Analysis*, p. 102444, 2022.
- [2] B. Stam, H. Peulen, M. M. Rossi, J. S. Belderbos, and J.-J. Sonke, "Validation of automatic segmentation of ribs for ntcp modeling," *Radiotherapy and Oncology*, vol. 118, no. 3, pp. 528–534, 2016.
- [3] S. Jang, P. M. Graffy, T. J. Ziemlewicz, S. J. Lee, R. M. Summers, and P. J. Pickhardt, "Opportunistic osteoporosis screening at routine abdominal and thoracic ct: normative ll trabecular attenuation values in more than 20 000 adults," *Radiology*, vol. 291, no. 2, pp. 360–367, 2019.
- [4] H. Shen, L. Liang, M. Shao, and S. Qing, "Tracing based segmentation for the labeling of individual rib structures in chest ct volume data," in *Proc. Int'l Conf. Medical Image Computing and Computer Assisted Intervention*. Springer, 2004, pp. 967–974.
- [5] T. Klinder, C. Lorenz, J. v. Berg, S. P. Dries, T. Bülow, and J. Ostermann, "Automated model-based rib cage segmentation and labeling in ct images," in *Proc. Int'l Conf. Medical Image Computing and Computer Assisted Intervention*. Springer, 2007, pp. 195–202.
- [6] J. Staal, B. van Ginneken, and M. A. Viergever, "Automatic rib segmentation and labeling in computed tomography scans using a general framework for detection, recognition and segmentation of objects in volumetric data," *Medical Image Analysis*, vol. 11, no. 1, pp. 35–46, 2007.
- [7] S. Ramakrishnan, C. Alvino, L. Grady, and A. Kiraly, "Automatic three-dimensional rib centerline extraction from ct scans for enhanced visualization and anatomical context," in *Proc. of SPIE Medical Imaging*, vol. 7962. SPIE, 2011, pp. 922–933.
- [8] D. Wu, D. Liu, Z. Puskas, C. Lu, A. Wimmer, C. Tietjen, G. Soza, and S. K. Zhou, "A learning based deformable template matching method for automatic rib centerline extraction and labeling in ct images," in *Proc. IEEE Conf. Computer Vision and Pattern Recognition*. IEEE, 2012, pp. 980–987.
- [9] M. Lenga, T. Klinder, C. Bürger, J. von Berg, A. Franz, and C. Lorenz, "Deep learning based rib centerline extraction and labeling," in *International Workshop on Computational Methods and Clinical Applications in Musculoskeletal Imaging*. Springer, 2018, pp. 99–113.
- [10] J. Yang, S. Gu, D. Wei, H. Pfister, and B. Ni, "Ribseg dataset and strong point cloud baselines for rib segmentation from ct scans," in *Proc. Int'l Conf. Medical Image Computing and Computer Assisted Intervention*. Springer, 2021, pp. 611–621.
- [11] J. Yao, S. D. O'Connor, and R. M. Summers, "Automated spinal column extraction and partitioning," in *3rd IEEE International Symposium on Biomedical Imaging: Nano to Macro, 2006*. IEEE, 2006, pp. 390–393.
- [12] T. Klinder, J. Ostermann, M. Ehm, A. Franz, R. Kneser, and C. Lorenz, "Automated model-based vertebra detection, identification, and segmentation in ct images," *Medical Image Analysis*, vol. 13, no. 3, pp. 471–482, 2009.
- [13] A. Sekuboyina, M. E. Husseini, A. Bayat, M. Löffler, H. Liebl, H. Li, G. Tetteh, J. Kukačka, C. Payer, D. Štern *et al.*, "Verse: a vertebrae labelling and segmentation benchmark for multi-detector ct images," *Medical Image Analysis*, vol. 73, p. 102166, 2021.
- [14] A. Vaswani, N. Shazeer, N. Parmar, J. Uszkoreit, L. Jones, A. N. Gomez, Ł. Kaiser, and I. Polosukhin, "Attention is all you need," *Advances in Neural Information Processing Systems*, vol. 30, 2017.
- [15] N. Carion, F. Massa, G. Synnaeve, N. Usunier, A. Kirillov, and S. Zagoryyko, "End-to-end object detection with transformers," in *Proc. European Conf. Computer Vision*. Springer, 2020, pp. 213–229.
- [16] Y. Zheng, A. Barbu, B. Georgescu, M. Scheuring, and D. Comaniciu, "Fast automatic heart chamber segmentation from 3d ct data using marginal space learning and steerable features," in *Proc. Int'l Conf. Computer Vision*. IEEE, 2007, pp. 1–8.
- [17] F. C. Ghesu, E. Krubasik, B. Georgescu, V. Singh, Y. Zheng, J. Hornegger, and D. Comaniciu, "Marginal space deep learning: efficient architecture for volumetric image parsing," *IEEE Trans. Medical Imaging*, vol. 35, no. 5, pp. 1217–1228, 2016.
- [18] L. Lu, A. Barbu, M. Wolf, J. Liang, L. Bogoni, M. Salganicoff, and D. Comaniciu, "Simultaneous detection and registration for ileocecal valve detection in 3d ct colonography," in *Proc. European Conf. Computer Vision*. Springer, 2008, pp. 465–478.
- [19] S. Ren, K. He, R. Girshick, and J. Sun, "Faster r-cnn: Towards real-time object detection with region proposal networks," *Advances in Neural Information Processing Systems*, vol. 28, 2015.
- [20] W. Liu, D. Anguelov, D. Erhan, C. Szegedy, S. Reed, C.-Y. Fu, and A. C. Berg, "Ssd: Single shot multibox detector," in *Proc. European Conf. Computer Vision*. Springer, 2016, pp. 21–37.
- [21] T.-Y. Lin, P. Goyal, R. Girshick, K. He, and P. Dollár, "Focal loss for dense object detection," in *Proc. Int'l Conf. Computer Vision*, 2017, pp. 2980–2988.
- [22] R. Girshick, F. Iandola, T. Darrell, and J. Malik, "Deformable part models are convolutional neural networks," in *Proc. IEEE Conf. Computer Vision and Pattern Recognition*, 2015, pp. 437–446.
- [23] X. Zhou, D. Wang, and P. Krähenbühl, "Objects as points," in *arXiv preprint arXiv:1904.07850*, 2019.
- [24] Z. Tian, C. Shen, H. Chen, and T. He, "Fcos: Fully convolutional one-stage object detection," in *Proc. Int'l Conf. Computer Vision*, 2019, pp. 9627–9636.
- [25] F. Isensee, P. F. Jaeger, S. A. Kohl, J. Petersen, and K. H. Maier-Hein, "nnu-net: a self-configuring method for deep learning-based biomedical image segmentation," *Nature methods*, vol. 18, no. 2, pp. 203–211, 2021.
- [26] K. He, G. Gkioxari, P. Dollár, and R. Girshick, "Mask r-cnn," in *Proc. Int'l Conf. Computer Vision*, 2017, pp. 2961–2969.

- [27] S. Liu, L. Qi, H. Qin, J. Shi, and J. Jia, "Path aggregation network for instance segmentation," in *Proc. IEEE Conf. Computer Vision and Pattern Recognition*, 2018, pp. 8759–8768.
- [28] K. Chen, J. Pang, J. Wang, Y. Xiong, X. Li, S. Sun, W. Feng, Z. Liu, J. Shi, W. Ouyang *et al.*, "Hybrid task cascade for instance segmentation," in *Proc. IEEE Conf. Computer Vision and Pattern Recognition*, 2019, pp. 4974–4983.
- [29] Y. Fang, S. Yang, X. Wang, Y. Li, C. Fang, Y. Shan, B. Feng, and W. Liu, "Instances as queries," in *Proc. Int'l Conf. Computer Vision*, 2021, pp. 6910–6919.
- [30] L. Jin, J. Yang, K. Kuang, B. Ni, Y. Gao, Y. Sun, P. Gao, W. Ma, M. Tan, H. Kang, J. Chen, and M. Li, "Deep-learning-assisted detection and segmentation of rib fractures from ct scans: Development and validation of fracnet," *EBioMedicine*, 2020.
- [31] N. Sharma, L. M. Aggarwal *et al.*, "Automated medical image segmentation techniques," *Journal of Medical Physics*, vol. 35, no. 1, p. 3, 2010.
- [32] D. Shen, G. Wu, and H.-I. Suk, "Deep learning in medical image analysis," *Annual Review of Biomedical Engineering*, vol. 19, p. 221, 2017.
- [33] F. Wang, K. Zheng, L. Lu, J. Xiao, M. Wu, and S. Miao, "Automatic vertebra localization and identification in ct by spine rectification and anatomically-constrained optimization," in *Proc. IEEE Conf. Computer Vision and Pattern Recognition*, 2021, pp. 5280–5288.
- [34] O. Ronneberger, P. Fischer, and T. Brox, "U-net: Convolutional networks for biomedical image segmentation," in *Proc. Int'l Conf. Medical Image Computing and Computer Assisted Intervention*. Springer, 2015, pp. 234–241.
- [35] Ö. Çiçek, A. Abdulkadir, S. S. Lienkamp, T. Brox, and O. Ronneberger, "3d u-net: learning dense volumetric segmentation from sparse annotation," in *Proc. Int'l Conf. Medical Image Computing and Computer Assisted Intervention*. Springer, 2016, pp. 424–432.
- [36] F. Milletari, N. Navab, and S.-A. Ahmadi, "V-net: Fully convolutional neural networks for volumetric medical image segmentation," in *Int'l Conf. on 3D Vision (3DV)*. IEEE, 2016, pp. 565–571.
- [37] M. Antonelli, A. Reinke, S. Bakas, K. Farahani, A. Kopp-Schneider, B. A. Landman, G. Litjens, B. Menze, O. Ronneberger, R. M. Summers *et al.*, "The medical segmentation decathlon," *Nature communications*, vol. 13, no. 1, pp. 1–13, 2022.
- [38] J. Ma, Y. Zhang, S. Gu, C. Zhu, C. Ge, Y. Zhang, X. An, C. Wang, Q. Wang, X. Liu *et al.*, "Abdomenct-1k: Is abdominal organ segmentation a solved problem," *IEEE Trans. Pattern Anal. Machine Intell.*, 2021.
- [39] P. Liu, Y. Deng, C. Wang, Y. Hui, Q. Li, J. Li, S. Luo, M. Sun, Q. Quan, S. Yang *et al.*, "Universal segmentation of 33 anatomies," *arXiv preprint arXiv:2203.02098*, 2022.
- [40] Y. Bian, Z. Zheng, X. Fang, H. Jiang, M. Zhu, J. Yu, H. Zhao, L. Zhang, J. Yao, L. Lu *et al.*, "Artificial intelligence to predict lymph node metastasis at ct in pancreatic ductal adenocarcinoma," *Radiology*, p. 220329, 2022.
- [41] X. Chen, R. Girshick, K. He, and P. Dollár, "Tensormask: A foundation for dense object segmentation," in *Proc. Int'l Conf. Computer Vision*, 2019.
- [42] X. Wang, T. Kong, C. Shen, Y. Jiang, and L. Li, "Solo: Segmenting objects by locations," in *Proc. European Conf. Computer Vision*, 2020.
- [43] B. Cheng, A. G. Schwing, and A. Kirillov, "Per-pixel classification is not all you need for semantic segmentation," *Advances in Neural Information Processing Systems*, 2021.
- [44] H. Wang, S. Sridhar, J. Huang, J. Valentin, S. Song, and L. J. Guibas, "Normalized object coordinate space for category-level 6d object pose and size estimation," in *Proc. IEEE Conf. Computer Vision and Pattern Recognition*, 2019, pp. 2642–2651.
- [45] J. Lin, Z. Wei, Z. Li, S. Xu, K. Jia, and Y. Li, "Dualposenet: Category-level 6d object pose and size estimation using dual pose network with refined learning of pose consistency," in *Proc. Int'l Conf. Computer Vision*, 2021, pp. 3560–3569.
- [46] Y. Weng, H. Wang, Q. Zhou, Y. Qin, Y. Duan, Q. Fan, B. Chen, H. Su, and L. J. Guibas, "Captra: Category-level pose tracking for rigid and articulated objects from point clouds," in *Proc. Int'l Conf. Computer Vision*, 2021, pp. 13 209–13 218.
- [47] J. Redmon, S. Divvala, R. Girshick, and A. Farhadi, "You only look once: Unified, real-time object detection," in *Proc. IEEE Conf. Computer Vision and Pattern Recognition*, 2016, pp. 779–788.
- [48] H. Law and J. Deng, "Cornernet: Detecting objects as paired keypoints," *Int. J. Computer Vision*, vol. 128, pp. 642–656, 2020.
- [49] X. Zhou, J. Zhuo, and P. Krähenbühl, "Bottom-up object detection by grouping extreme and center points," in *Proc. IEEE Conf. Computer Vision and Pattern Recognition*, 2019.
- [50] Z. Yang, S. Liu, H. Hu, L. Wang, and S. Lin, "Reppoints: Point set representation for object detection," in *Proc. Int'l Conf. Computer Vision*, 2019.
- [51] X. Zhu, W. Su, L. Lu, B. Li, X. Wang, and J. Dai, "Deformable detr: Deformable transformers for end-to-end object detection," in *Proc. Int'l Conf. Learning Representations*, 2021.
- [52] P. Sun, R. Zhang, Y. Jiang, T. Kong, C. Xu, W. Zhan, M. Tomizuka, L. Li, Z. Yuan, C. Wang, and P. Luo, "Sparse r-cnn: End-to-end object detection with learnable proposals," in *Proc. IEEE Conf. Computer Vision and Pattern Recognition*, 2021.
- [53] I. Misra, R. Girdhar, and A. Joulin, "An end-to-end transformer model for 3d object detection," in *Proc. Int'l Conf. Computer Vision*, 2021, pp. 2906–2917.
- [54] R. B. Glass, K. I. Norton, S. A. Mitre, and E. Kang, "Pediatric ribs: a spectrum of abnormalities," *Radiographics*, vol. 22, no. 1, pp. 87–104, 2002.
- [55] K. He, X. Zhang, S. Ren, and J. Sun, "Deep residual learning for image recognition," in *Proc. IEEE Conf. Computer Vision and Pattern Recognition*, 2016, pp. 770–778.
- [56] I. T. Jolliffe and J. Cadima, "Principal component analysis: a review and recent developments," *Philosophical Transactions of the Royal Society A: Mathematical, Physical and Engineering Sciences*, vol. 374, no. 2065, p. 20150202, 2016.
- [57] H. W. Kuhn, "The hungarian method for the assignment problem," *Naval research logistics quarterly*, vol. 2, no. 1-2, pp. 83–97, 1955.
- [58] H. Rezatofighi, N. Tsoi, J. Gwak, A. Sadeghian, I. Reid, and S. Savarese, "Generalized intersection over union: A metric and a loss for bounding box regression," in *Proc. IEEE Conf. Computer Vision and Pattern Recognition*, 2019, pp. 658–666.
- [59] Y. Deng, C. Wang, Y. Hui, Q. Li, J. Li, S. Luo, M. Sun, Q. Quan, S. Yang, Y. Hao *et al.*, "Ctspine1k: A large-scale dataset for spinal vertebrae segmentation in computed tomography," *arXiv preprint arXiv:2105.14711*, 2021.
- [60] A. Paszke, S. Gross, F. Massa, A. Lerer, J. Bradbury, G. Chanan, T. Killeen, Z. Lin, N. Gimelshein, L. Antiga *et al.*, "Pytorch: An imperative style, high-performance deep learning library," *Advances in Neural Information Processing Systems*, vol. 32, 2019.
- [61] K. Chen, J. Wang, J. Pang, Y. Cao, Y. Xiong, X. Li, S. Sun, W. Feng, Z. Liu, J. Xu *et al.*, "Mmdetection: Open mmlab detection toolbox and benchmark," *arXiv preprint arXiv:1906.07155*, 2019.
- [62] I. Loshchilov and F. Hutter, "Decoupled weight decay regularization," *arXiv preprint arXiv:1711.05101*, 2017.
- [63] H.-Y. Zhou, J. Guo, Y. Zhang, L. Yu, L. Wang, and Y. Yu, "nnformer: Interleaved transformer for volumetric segmentation," *arXiv preprint arXiv:2109.03201*, 2021.
- [64] Y. Tang, D. Yang, W. Li, H. R. Roth, B. Landman, D. Xu, V. Nath, and A. Hatamizadeh, "Self-supervised pre-training of swin transformers for 3d medical image analysis," in *Proc. IEEE Conf. Computer Vision and Pattern Recognition*, 2022, pp. 20 730–20 740.
- [65] H. Hu, J. Gu, Z. Zhang, J. Dai, and Y. Wei, "Relation networks for object detection," in *Proc. IEEE Conf. Computer Vision and Pattern Recognition*, 2018, pp. 3588–3597.
- [66] M. Musy, G. Jacquenot, and G. Dalmaso, "vedo, a python module for scientific analysis and visualization of 3d objects and point clouds," [doi:10.5281/zenodo.5655358](https://doi.org/10.5281/zenodo.5655358), 2021.
- [67] W. Liu, Y. Wang, T. Jiang, Y. Chi, L. Zhang, and X.-S. Hua, "Landmarks detection with anatomical constraints for total hip arthroplasty preoperative measurements," in *Proc. Int'l Conf. Medical Image Computing and Computer Assisted Intervention*. Springer, 2020, pp. 670–679.
- [68] X. Chen, S. Xie, and K. He, "An empirical study of training self-supervised vision transformers," in *Proc. IEEE Conf. Computer Vision and Pattern Recognition*, 2021, pp. 9640–9649.
- [69] C. Tobon-Gomez, T. Stroud, J. Cameron, D. Elcock, A. Murray, D. Wyeth, C. Conway, S. Reynolds, P. A. G. Teixeira, A. Blum *et al.*, "Unfolded cylindrical projection for rib fracture diagnosis," in *International Workshop on Computational Methods and Clinical Applications in Musculoskeletal Imaging*. Springer, 2017, pp. 36–47.

APPENDICES

A. RibInst Dataset Construction

Iterative Annotation. First of all, we have to get well-annotated binary rib segmentation mask for each volume even if manually annotating voxels in 3D space is a time-consuming, labor-intensive task. We adopted an automatic tool to improve the annotating efficiency, which has an operating pipeline of 1) separating bones using thresholding and morphology operations, 2) removing the spine and the sternum, and 3) distinguishing rib from other remaining bones with a pre-trained machine learning model. Using this tool, we collected 50 coarse masks with hollow components, thus binary closing operation was performed on each mask to include rib marrow regions. Two radiologists manually removed the cartilago costalis and refined the boundaries between ribs and spine for each scan. Then, we trained one U-Net [34] and predicted foregrounds (rib masks) for another 50 cases among unannotated scans using the trained model, followed by a new round of manual refinement. After several rounds of this iterative annotation process, we obtained high-quality binary segmentation for all ribs in this dataset.

Instance Labeling. Given the binary segmentation, we wish to efficiently set a unique label per rib in each CT scan. An interactive annotation tool was developed to fulfill this goal. The label for each rib within one connected component is determined by one click and the following entered number. The maximal number was set to 24, as 12 pairs of ribs may present at most common scans, 5%-8% of normal individuals may have 11 pairs, while supernumerary ribs may rarely be seen as normal variant according to [54]. The instance label for each rib increases in the order of top to bottom and right to left in the patient view.

Quality Control. Despite its high efficiency of the instance labeling tool, it is hard (if not impossible) to avoid mistakes when observing and labeling in 3D space, especially for identifying elongated and oblique objects such as ribs. Thus it is essential to perform quality control to improve and assure the overall annotation quality. All labeled masks were projected into 2D space via cylindrical projection [69] to obtain visually intuitive demonstrations. Rib labels were mapped to common strings for the sake of readability and attached to the corresponding ribs. Misabeled ribs or bad segmented components were easy to be distinguished in this 2D image. When mistakes were found, we turned back to previous stages to manually repair the segmentation masks or correct the labels. Some visualizations of intermediate results during the instance annotation and quality control process are shown in Fig. 8.

B. RibInst Attributes

Various FOVs & Statistics. RibInst consists of 654 chest-abdomen CT scans, of which FOVs vary greatly. Fig. 7 shows three typical types of FOVs in RibInst. The region of ribcage can locate in various area of the whole volume, thus the preceding ROI extractor can help Med-Query concentrated in the targeted region. Specific statistic information of different subsets in RibInst is depicted in Table VI.

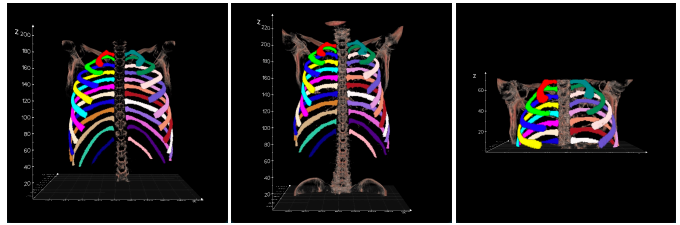


Fig. 7. Three typical types of FOVs in RibInst. The relative position of the targeted region in the image coordinate system vary greatly.

TABLE VI
The number of CT scans and annotated ribs in RibInst.

Splits	#CT Scans	#Ribs
Train	420	10035
Validation	74	1729
Test	160	3764
Total	654	15528

C. Segmentation Metrics in Details

Denoting the ground-truth by T and the corresponding prediction by P , and indexing the anatomies with i , we compute the mean Dice score across the target anatomies per scan as follows:

$$\text{DSC}(P, T) = \frac{1}{N} \sum_{i=1}^N \frac{2|P_i \cap T_i|}{|P_i| + |T_i|}. \quad (4)$$

As for surface measures, we adopt HD95 and ASSD. The mean of maximum HD over all ribs is defined as:

$$\text{HD}(P, T) = \frac{1}{N} \sum_{i=1}^N \max \left\{ \sup_{p \in \mathcal{P}_i} \inf_{t \in \mathcal{T}_i} d(p, t), \sup_{t \in \mathcal{T}_i} \inf_{p \in \mathcal{P}_i} d(p, t) \right\}, \quad (5)$$

where \mathcal{P}_i and \mathcal{T}_i denote the surfaces extracted from the voxel masks of the i^{th} rib and $d(p, t) = \|p - t\|_2$, i.e., a Euclidean distance between the points p and t on the two surfaces. HD95 is slightly different from maximum HD in that it calculates the 95th percentile of the shortest distances between surface points to alleviate the impact of outliers. Similarly, ASSD is defined as:

$$\text{ASSD}(P, T) = \frac{1}{2N} \sum_{i=1}^N \left(\frac{1}{|\mathcal{P}_i|} \sum_{p \in \mathcal{P}_i} \inf_{t \in \mathcal{T}_i} d(p, t) + \frac{1}{|\mathcal{T}_i|} \sum_{t \in \mathcal{T}_i} \inf_{p \in \mathcal{P}_i} d(p, t) \right). \quad (6)$$

As discussed in the main text, HD and ASSD are not defined for missing anatomies. We follow the practice of [13] to ignore such anatomies while computing the averages.

D. Relative Distance Constraints

To impose more geometrical constraints, we explore additional relative distance constraints between center points of the 9-DoF boxes. Defining the $\Delta x_i^p = x_i^p - x_{i-1}^p$, and $\Delta \hat{x}_i^p = \hat{x}_i^p - \hat{x}_{i-1}^p$, we compute a relative distance term as $\|\Delta \hat{x}_i^p - \Delta x_i^p\|_1$, slightly different from [67]. For rib parsing,

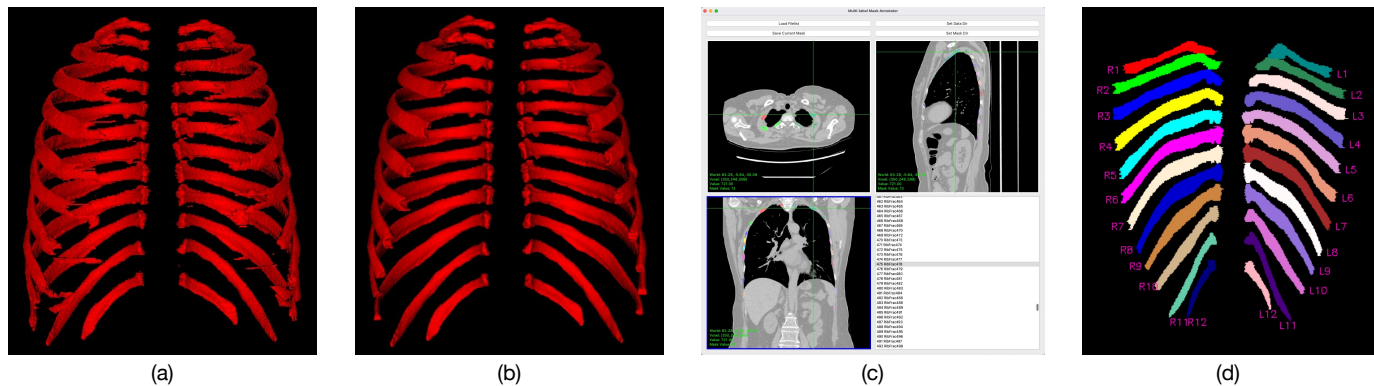


Fig. 8. (a) A binary segmentation mask in the early stage. (b) A refined version after iterative annotation. (c) The user interface of the interactive instance labeling tool. (d) An unfolded cylindrical projection in 2D space for quality control.

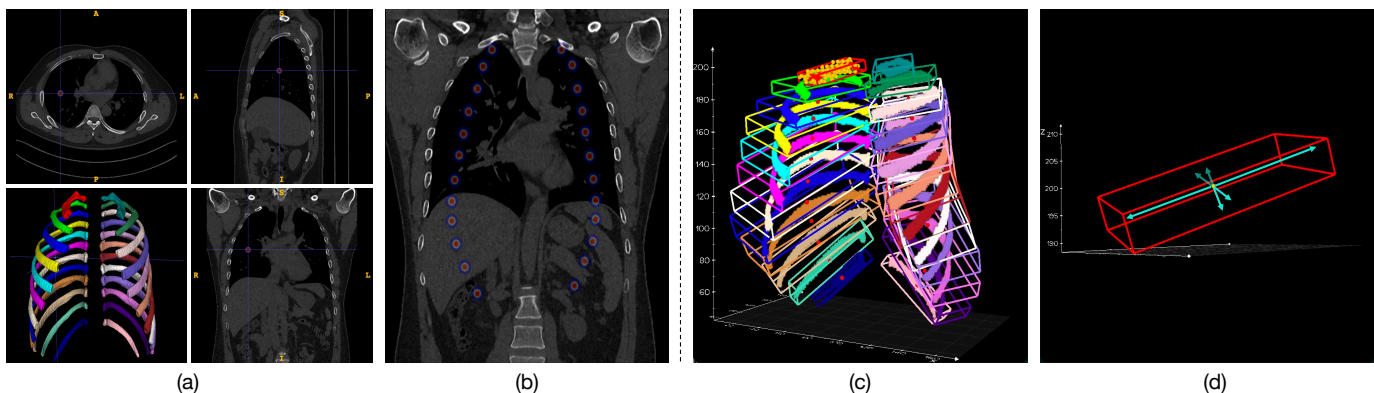


Fig. 9. Visual illustration about the critical adaptations. CenterNet: (a) One target center in three orthogonal views and 3D rendering; (b) All target centers are projected into one cross-section in coronal view via maximum intensity projection. FCOS: (c) Points inside the 9-DoF box are chosen as positive samples, e.g., golden points inside the 1st right rib box; (d) The relative offsets from the six sides of the 9-DoF box to the point location are its scale regression targets.

since *RandomCrop* may change the continuity of the rib sequence, the weight of this term for ribs that do not have an adjacent preceding rib, will be set as zero.

E. Critical Adaptations of CenterNet & FCOS

Based on RibInst, we describe the critical adaptations to introduce two popular anchor-free CNN detectors into the 9-DoF box detection task.

CenterNet. In our CenterNet [23] implementation, object center detection task is formulated as detecting the center of the parameterized 9-DoF box for each rib. Each center is represented as a 3D Gaussian heatmap with an appropriate kernel size. Heatmaps for all ribs are assembled in channel dimension to form a 4D tensor per scan. Visual illustrations are shown in Fig. 9(a)(b).

FCOS. In our FCOS [24] implementation, the critical challenge is to find proper positive samples for obliquely oriented ribs in 3D space. For each rib, points inside the 9-DoF box representation in the local coordinate system will be sampled as positive anchor points. For each anchor point, the offsets from the six sides of the box to its location are set as the scale regression targets, as shown in Fig. 9(c)(d).

F. Rib-level Comparison between nnU-Net and Med-Query

A rib-level instance segmentation performance comparison between nnU-Net [25] and Med-Query is shown in Fig. 10. We can see that the performances of nnU-Net on intermediate ribs (i.e., from R2 to R11 and from L2 to L11) vary more than Med-Query. It reflects that correctly and precisely identifying the intermediate ribs is indeed hard due to their similar appearances and contextual surroundings. Patch-based training strategy lacks of global information so that results in noticeable label confusion. Although expanding the patch size can alleviate this problem to some degree, it will fall into the dilemma of extremely increased GPU memory. On the contrary, Med-Query optimizes the detection-then-segmentation paradigm for 3D CT scans in which it detects on low resolution with global FOV and segments on high resolution with local FOV.

G. More Qualitative Results

We demonstrate more qualitative results on RibInst in Fig. 11 and abdominal multi-organ segmentation results on FLARE22 in Fig. 12. Compared to baseline methods (including centerline-based, detection-based and segmentation-based methods), Med-Query shows its robustness of distinguishing and segmenting instances of anatomical structures.

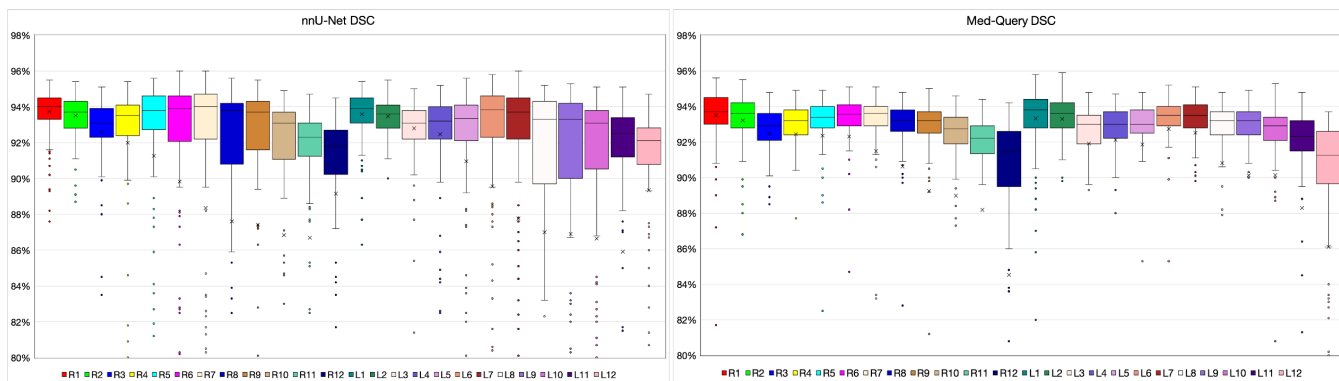


Fig. 10. Rib-level segmentation performance comparison between nnU-Net and Med-Query. “R” means right ribs and “L” means left ribs.

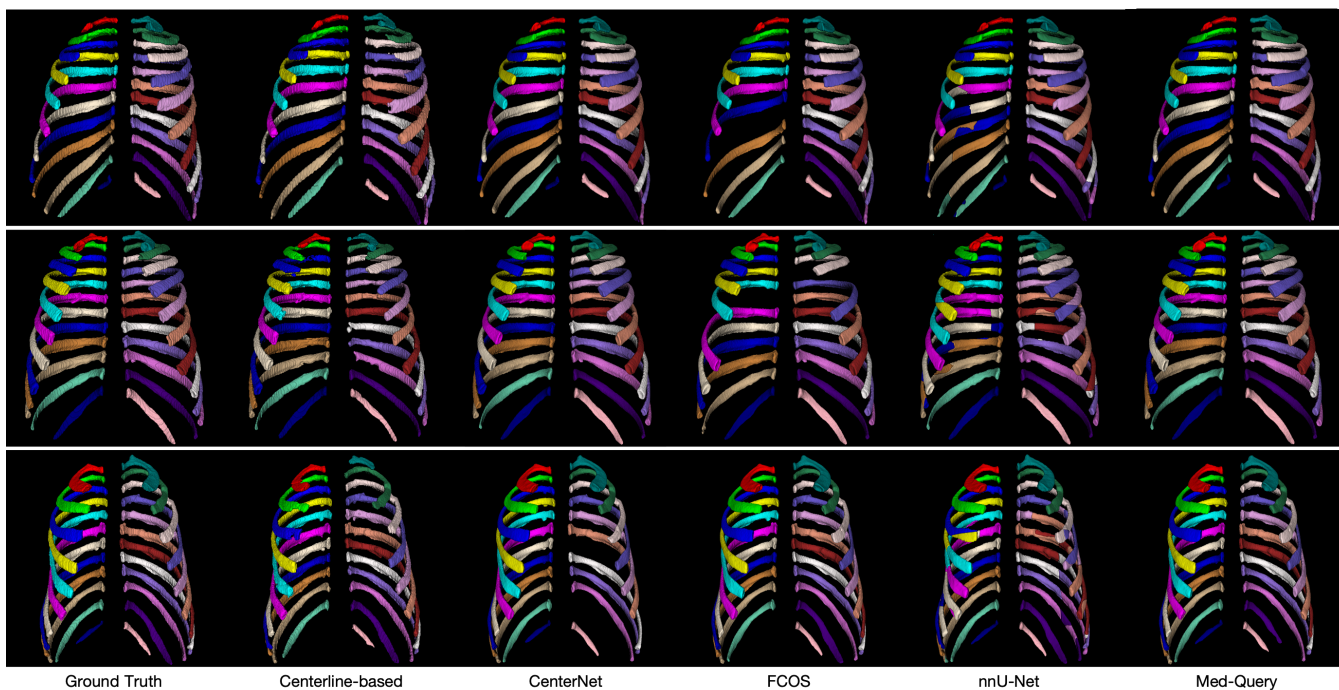


Fig. 11. 3D volume renderings of rib instance segmentation and labeling results of Med-Query and the strong baseline methods.

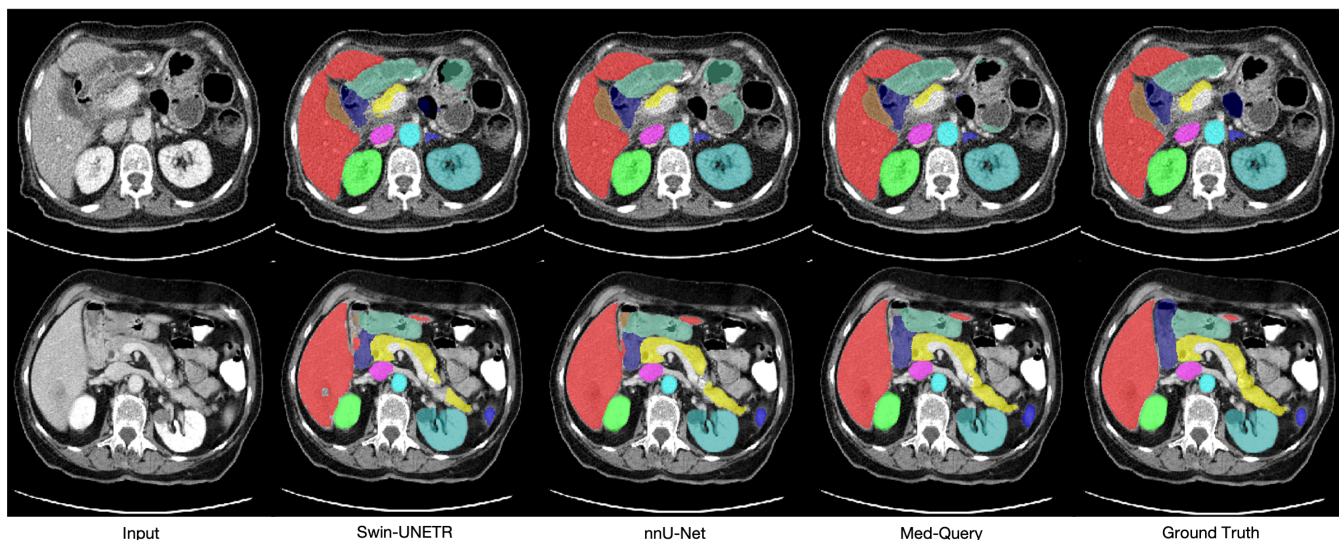


Fig. 12. Two cases of qualitative abdominal multi-organ segmentation results on FLARE22 validation set. Best viewed in color.